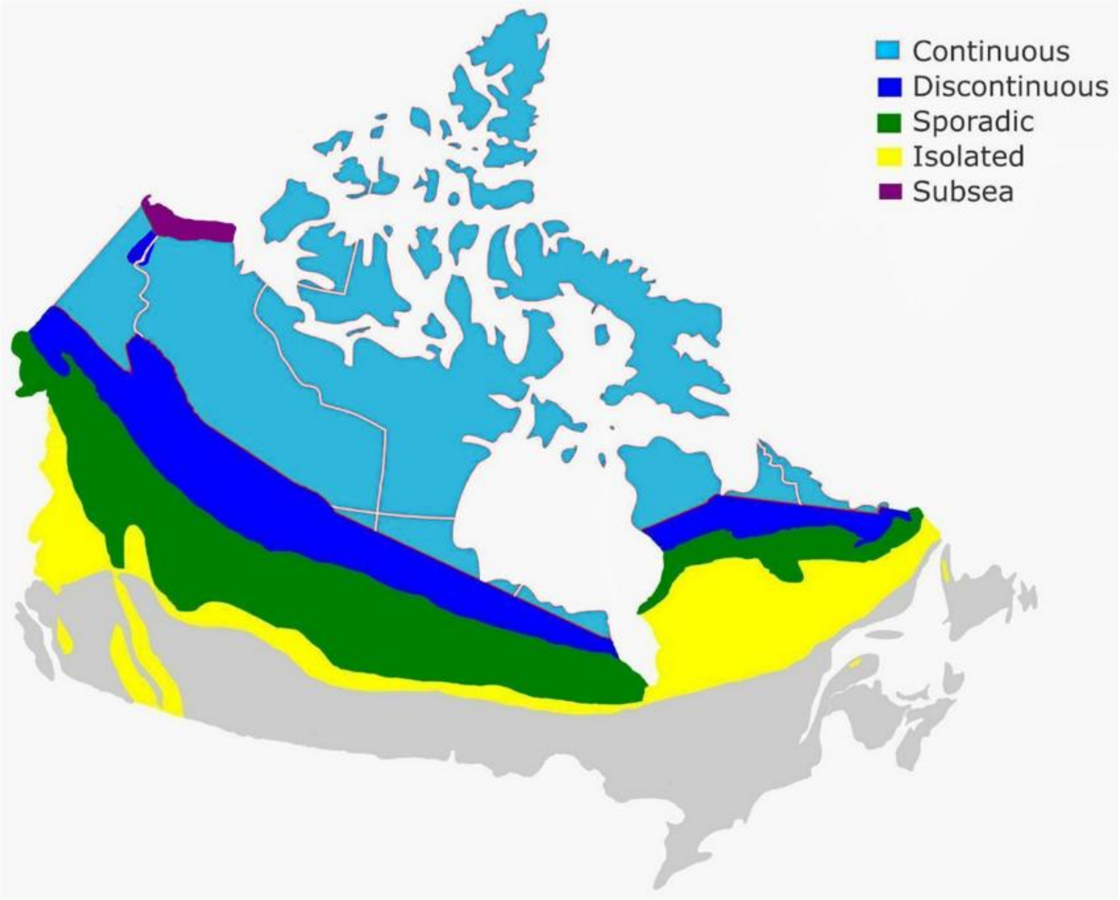

**3rd year project report (2025-2026)**

# Numerical modelling of the permafrost thawing and its repercussions in the Northwest Territories

**Aram Moradi and Vadim Kravchinsky ***

***Institute for Geophysical Research, Department of Physics, University of Alberta***

**March 2026**

*Correspondence to vadim@ualberta.ca

## Abstract

Permafrost, which underlies about one quarter of the Northern Hemisphere, is rapidly degrading in the Northwest Territories (NWT), particularly in the Mackenzie River Delta (MRD) and along the Inuvik–Tuktoyaktuk Highway (ITH) corridor. This study develops and validates an observation-driven Machine Learning (ML) framework to map spatial and temporal variability in MAGT and ALT in the MRD–ITH study area in the Northwest Territories using a decade of borehole temperature data and environmental predictors. Random Forest and Neural Network models produced high-resolution predictions with strong agreement to field observations, demonstrating robust spatial and temporal generalization, with uncertainty highest in ecotonal and heterogeneous terrain.

Spatial analyses indicate that vegetation cover, proximity to water bodies, and terrain characteristics strongly modulate permafrost thermal regimes. Shallow Active Layer Thickness (ALT) and colder Mean Annual Temperature (MAGT) dominate tundra and upland zones, whereas deeper seasonal thaw and warmer ground temperatures occur in southern lowlands and forested regions. Comparison between two partially overlapping five-year periods (2013–2018 and 2018–2023) reveals measurable decadal warming and active-layer deepening across the MRD–ITH study area, with pronounced change along transportation corridors and deltaic environments. Difference maps and rate-based heatmaps identify emerging thaw hotspots, demonstrating that both absolute thermal thresholds and rates of change are critical early warning indicators of permafrost instability.

The modelling framework assumes stationary relationships between predictors and ground thermal state and does not explicitly simulate subsurface thermodynamics; therefore, results represent spatially informed statistical predictions rather than process-based simulations. Nonetheless, integrating extensive field observations with ML techniques provides an observation-constrained baseline for regional permafrost monitoring. Future work will extend this framework to scenario-based projections using Representative Concentration Pathways (RCPs) and downscaled climate projections to 2100 and beyond, enabling quantitative assessment of infrastructure risk, carbon feedbacks, and long-term permafrost vulnerability in a rapidly warming Arctic.

## 1. Introduction

Permafrost underlies about one quarter of the Northern Hemisphere and plays a critical role in Arctic ecosystems, infrastructure stability, and global carbon storage (1–4). Its thermal stability is highly sensitive to rising air temperatures, snow cover dynamics, and vegetation change. Thawing permafrost destabilizes landscapes, threatens northern communities, and releases greenhouse gases, amplifying climate change (5–7). Therefore, accurate representation of present-day permafrost thermal conditions is essential for impact projections and for initializing and validating predictive models (8, 9).

MAGT and ALT are key indicators of permafrost stability, governing year-round ground freezing and seasonal thaw depth (10–13). These indicators influence carbon storage, infrastructure integrity, and ecosystem processes. Because they respond to interacting controls such as climate, vegetation, topography, soil properties, snow insulation, soil thermal conductivity, and moisture dynamics, they are well suited to ML approaches (14–20). Accelerated Arctic warming further complicates ALT prediction, particularly in climate-sensitive regions like Canada’s NWT, which contains extensive carbon-rich permafrost.

Conventional MAGT and ALT mapping methods often depend on sparse observations, coarse climate inputs, and simplified physical assumptions, leading to underrepresentation of fine-scale heterogeneity and thaw hotspots (21–27). These limitations affect downstream estimates of carbon emissions, hydrology, and infrastructure vulnerability (28, 29). Although **physically based** models such as GIPL2 and CryoGrid simulate energy and hydrological processes, their computational demands and limited scalability restrict high-resolution regional applications (30-32).

Recent ML advances enable integration of diverse environmental datasets and capture nonlinear relationships among permafrost controls (30–33). Algorithms such as Random Forests (RF), Support Vector Machines, and Neural Networks (NNs) have shown promise in predicting thermokarst development, ground settlement, and subsurface thermal conditions using remote sensing, borehole, and reanalysis data (34, 35). However, many studies operate at continental or global scales, where sparse high-latitude observations reduce generalizability and obscure local variability (34–36). Nevertheless, ML methods effectively capture complex interactions among vegetation, topography, soil moisture, and climate, supporting high-resolution, spatially continuous predictions relevant to adaptation and infrastructure planning (37, 38).

This study focuses on the MRD and the ITH corridor in the western Canadian Arctic (39, 40). The MRD is an ice-rich, carbon-bearing deltaic system, while the ITH traverses tundra, peatlands, glaciated plateaus, and coastal environments. The region is characterized by moderate to very high ground ice content, thick permafrost (>100–500 m), and typically shallow ALT (<1 m), with strong local variability (2). The climate is continental, with historically low mean annual air temperatures and increasing warming trends exceeding 2.5 °C since the 1970s, alongside substantial snowfall variability (41). These gradients create a climate-sensitive transition zone between boreal and Arctic systems (2, 39, 40, 42–45).

We evaluate whether observation-driven ML models can resolve fine-scale spatial variability in permafrost thermal state and detect recent warming and thaw trends unresolved by existing maps. Using 79 monitoring sites and a decade of observations (2013–2023), we produce high-resolution, spatially continuous maps of MAGT and ALT across MRD–ITH study area in the NWT and assess changes between 2013–2018 and 2018–2023. The study region includes the MRD, where deepening thaw, subsidence, and methane emissions have been documented (46). By quantifying spatial variability and uncertainty across ecotones, this work provides observation-constrained baselines to improve projections of permafrost change, climate–carbon feedbacks, and infrastructure risk in a rapidly warming Arctic.

Environmental predictors include climate variables (air temperature, precipitation, snow cover, thawing and freezing degree days), vegetation type and cover, soil properties (texture, organic carbon), hydrological indicators (moisture, water content), and topographic indices (elevation, slope, aspect), enabling integrated modeling of the key biophysical controls on MAGT and ALT.

## 2. Goals

The three main goals of our project leverage the transformative potential of ML models to enhance permafrost research and thawing forecasting in the MRD-ITH:

**Goal 1:** Develop and validate ML models for predicting permafrost thermal indicators. This objective focuses on applying RF and NNs models to predict MAGT and ALT using environmental, climatic, and geotechnical predictors derived from borehole observations. The goal is to establish a robust observation-driven framework that can support spatially continuous predictions of ground thermal conditions across the study area.

**Goal 2:** Map the spatial distribution of permafrost thermal conditions and identify areas of elevated thaw risk. Using the trained ML models, high-resolution maps of MAGT and ALT are generated to characterize the spatial variability of permafrost conditions across the MRD–ITH region. Particular attention is given to areas containing infrastructure, including drilling mud sumps and transportation corridors, where thaw-induced ground instability may pose environmental and engineering risks.

**Goal 3:** Detect recent changes in permafrost thermal state and evaluate model robustness. This objective assesses temporal changes in permafrost conditions by comparing two partially overlapping time periods (2013–2018 and 2018–2023). The analysis evaluates decadal trends in MAGT and ALT, identifies emerging thaw hotspots, and tests the spatial and temporal generalization of the ML models through cross-validation and environmental transferability analyses.

## 3. Data and Methods

### 3.1 Data

This study uses detailed in situ ground temperature data collected along the ITH corridor (Fig. 1) over a decade. The monitoring network includes sentinel, embankment, alignment, and creek bank boreholes installed across different terrain types, including hilltops, riparian zones, and peatlands. These regions are underlain by continuous, ice-rich permafrost, with thickness ranging from approximately 100 m near Inuvik to more than 500 m near Tuktoyaktuk. Thermistor strings installed in the boreholes record ground temperature at multiple depths, allowing assessment of thermal conditions within road embankments and the underlying permafrost.

ALT is estimated from the depth at which ground temperature crosses 0 °C at each site. However, the precision of ALT estimates derived from thermistor strings depends on the vertical spacing of sensors, which constrains the resolution at which the thaw depth can be identified. While this approach provides consistent, multi-year estimates of thaw penetration, the most precise measurements of ALT are typically obtained through direct end-of-season field probing of the depth to frozen ground in late autumn, just prior to sustained sub-zero air temperatures. MAGT is determined from depths where seasonal temperature fluctuations are minimal, typically below ~10 m.

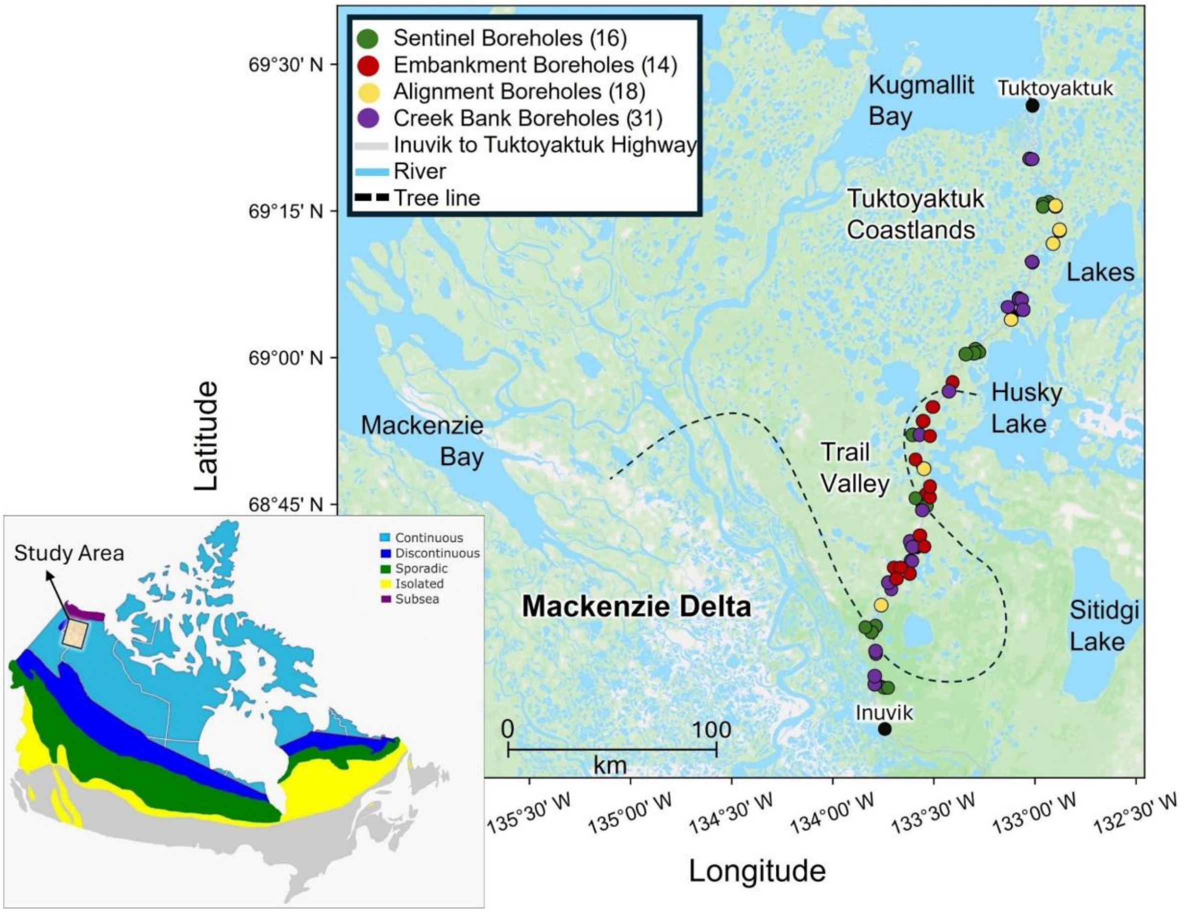

**Fig. 1. Study area (MRD-ITH) in the NWT, Canada. Permafrost zones across Canada.** The study region in the NWT is shown within the continuous and discontinuous zones (**Left**). Locations of 79 boreholes along the ITH and MRD, used for modeling MAGT and ALT across diverse terrain types (**Right**).

In addition to thermal observations, geological and geotechnical data were compiled for the same region, including soil texture (sand, silt, clay), moisture content, liquid water content, soil organic carbon (SOC), dissolved organic carbon (DOC), slope, aspect, longitude, latitude, elevation, and vegetation cover. Vegetation transitions from open woodland near Sitidgi Lake in the south to low shrub tundra further north, culminating in coastal tundra communities. Climate data were obtained from Environment and Climate Change Canada stations representing three major subregions (Inuvik, Trail Valley, and Tuktoyaktuk), including air temperature, precipitation, and snow depth. From air temperature records, thawing degree days

(TDD) and freezing degree days (FDD) were calculated and incorporated as additional climatic predictors (40-43, 47-49).

## 3.2 Methods

### 3.2.1 Machine learning model design

To predict MAGT and ALT, we applied two complementary ML approaches: RF and NNs. To model permafrost thaw indicators across the MRD–ITH study area, two ML algorithms, RF and NNs, were implemented using historical field data. The modeling framework was designed to predict MAGT and ALT using supervised learning techniques. These approaches were selected based on their established capacity to handle nonlinear relationships, manage high-dimensional inputs, capture spatial heterogeneity, and deliver robust predictions across complex environmental settings. RF was chosen for its interpretability and performance in data-sparse areas, while NNs were employed for their ability to model nonlinear interactions among high-dimensional input features in more data-rich domains. Their combined use ensures both accuracy and resilience, enhancing model confidence through cross-method agreement (50, 51).

### 3.2.2 Data preparation and feature set

Before model training, preprocessing steps including imputation of missing data, handling of inconsistent entries, and standardization of feature scales were conducted (52, 53). Prior to modeling, ML-based imputation procedures were used for incomplete records, ensuring consistency across time series and site-specific measurements (54). Variables were standardized to normalize distributions and minimize scale-related bias.

Input features for both models comprised the full set of environmental, geotechnical, and climatic variables described above. These included climatic variables (air temperature, precipitation, snow cover, TDD, FDD), geotechnical properties (soil texture, moisture content, SOC, DOC, liquid water content), environmental variables (vegetation type and cover), and topographic attributes (longitude, latitude, elevation, slope, and aspect). This represents a comprehensive set of predictors capturing the primary environmental controls on permafrost thermal dynamics, although it does not exhaustively include all possible drivers such as disturbance events, subsurface hydrology, or detailed surface energy balance processes. Key input variables include soil thermal properties, such as moisture content (MC), snow ground (SG), TDD, FDD, air temperature (AT), precipitation (Pre), vegetation (Veg), longitude (Lon), latitude (Lat), SOC, DOC, soil properties (Spro), liquid water (Liq_water) and topographic features, including elevation (Ele), slope, and aspect. These features are selected based on their established influence on permafrost thermal dynamics. The effects of variables on MAGT and ALT, our models were designed using the following equations (56):

$$MAGT = f_1(TDD) + f_2(FDD) + f_3(MC) + f_4(SG) + f_5(Pre) + f_6(SOC) + f_7(Lon) + f_8(Lat) + + f_9(Ele) + f_{10}(DOC) + f_{11}(Veg) + f_{12}(Aspect) + f_{13}(Liq_{water}) + + f_{14}(Spro) + f_{15}(AT) + f_{16}(Slope)$$

$$ALT = f_1(TDD) + f_2(FDD) + f_3(MC) + f_4(SG) + f_5(Pre) + f_6(SOC) + f_7(Lon) + f_8(Lat) + + f_9(Ele) + f_{10}(DOC) + f_{11}(Veg) + f_{12}(Aspect) + f_{13}(Liq_{water}) + + f_{14}(Spro) + f_{15}(AT) + f_{16}(Slope)$$

### 3.2.3 Training and validation design

Model robustness was evaluated using a 10-fold cross-validation (k = 10) strategy. The dataset was randomly partitioned into ten subsets of approximately equal size. In each iteration, nine subsets (90% of the data) were used for training, while the remaining subset (10%) served as the validation set. This process was repeated ten times so that each subset was used once as the validation data.

To further assess spatial generalization, an additional leave-site-out validation was conducted. In this approach, all observations from a given monitoring site were excluded from model training and used only for validation. This procedure tests the ability of the model to predict permafrost conditions at previously unseen monitoring locations and reduces the risk of spatial leakage between training and validation samples.

Model performance was evaluated using root mean square error (RMSE), correlation coefficient ($R^2$), and mean difference (bias) between observed and predicted values (55, 56).

### 3.2.4 Environmental-block validation and domain of applicability

To assess model transferability beyond the immediate conditions represented by individual monitoring sites, we applied an environmental-block validation scheme. Samples were grouped into environmental blocks by clustering observations in the multivariate covariate space using K-means, based on the full set of predictors used in the ML models. During validation, entire clusters were withheld from training and used as independent test sets. This design provides a stricter assessment of model generalization than random cross-validation because it evaluates performance under environmental conditions that are less similar to those used for model fitting. In parallel, we assessed the domain of applicability of the trained models using covariate-range coverage and nearest-neighbor distance-based familiarity metrics. These diagnostics identify locations where predictions are supported by conditions well represented in the training data and distinguish them from areas where extrapolation risk is higher.

### 3.2.5 Random forest implementation

RF is an ensemble-based algorithm that constructs multiple decision trees using bootstrap aggregation and random feature selection at each node split. This twofold randomness reduces overfitting and increases model stability (57). The algorithm's out-of-bag (OOB) estimation further enables error assessment without requiring an additional validation set, while also ranking feature importance.

The RF algorithm was selected for its ensemble-learning structure, which builds multiple decision trees from bootstrap samples and random feature subsets to generate robust regression predictions. Each tree was independently trained using different combinations of samples and predictors, thereby reducing overfitting through internal decorrelation (58).

In this study, RF was trained using bootstrap samples and optimized for regression to predict MAGT and ALT. OOB samples were used to estimate generalization error internally (59). Prediction accuracy was assessed using RMSE, $R^2$, and bias metrics (60), and validated against observed values from the validation datasets.

### 3.2.6 Neural networks implementation

NNs were constructed as fully connected feed-forward networks comprising an input layer, two hidden layers with nonlinear activation functions, and an output node representing the predicted MAGT or ALT value. The input layer received the full feature set described above, while the hidden layers captured complex interdependencies among geotechnical, climatic, and environmental attributes. To reduce overfitting, dropout regularization was applied between hidden layers, where neurons are randomly deactivated during training. The final output layer consisted of a single node producing the predicted MAGT or ALT value, depending on the modeling target (61).

The NNs were trained using backpropagation to iteratively adjust network weights and minimize prediction error by optimizing the loss function (61, 62). Input variables mirrored those used in the RF model to allow direct comparison between algorithms. Model performance was evaluated using the same cross-validation and leave-site-out validation procedures described above.

The architecture allows the network to learn complex nonlinear relationships among soil, vegetation, and climate variables that influence permafrost thermal dynamics (62–64). While RF offered higher interpretability and clearer feature importance rankings, NNs provided a flexible framework for modeling latent interactions and capturing nonlinear environmental behavior. Together, these models enabled robust and complementary assessments of permafrost thermal state across the MRD–ITH study area, where spatial coverage of ground observations remains limited (65, 66).

## 4. Results

In this reporting year of this study, RF and NNs successfully predicted MAGT and ALT across monitoring sites in the MRD- ITH study area in the NWT using long-term geotechnical, climatic, and environmental data. While RF provided robust variable selection and resistance to overfitting, NNs better captured complex nonlinear interactions and achieved higher overall accuracy, with both models demonstrating strong agreement with field observations and confirming the reliability of the mapping framework across heterogeneous Arctic landscapes. We further produced high-resolution spatial maps of predicted MAGT to characterize its distribution across the study area. This year, ML model robustness was further evaluated using a station-group (leave-site-out) cross-validation, temporal transfer tests between 2013–2018 and 2018–2023, and environmental-block validation.

### 4.1 Spatial and Temporal Generalization and Environmental Transferability

Station-group (leave-site-out) validation showed that when entire monitoring stations were excluded from training, the ML model maintained strong predictive performance for both MAGT and ALT, demonstrating robust spatial generalization to previously unseen locations without spatial leakage (Table 1).

**Table 1.** Model performance under station-group (leave-site-out) cross-validation for MAGT and ALT.

| Validation | RMSE | MAE | Bias |
|---|---|---|---|
| **MAGT** | 0.59 | 0.48 | -0.01 |
| **ALT** | 0.38 | 0.31 | 0.02 |

Temporal transfer testing further evaluated model stability under recent climate variability by training on one five-year period and testing on the subsequent period (and vice versa), assessing the model's ability to remain reliable under shifting climatic conditions (Table 2).

**Table 2.** Temporal transfer test results for the ML model trained on the first five-year periods (2013-2018) and tested on the second (2018–2023), and vice versa, to evaluate predictive stability under recent climate change.

| Validation | RMSE | MAE | $R^2$ | Bias |
|---|---|---|---|---|
| **Train:2013-2018**<br>**Test:2018-2023**<br>**MAGT** | 0.58 | 0.45 | 0.65 | 0.03 |
| **Train: 2018-2023**<br>**Test: 2013-2018**<br>**MAGT** | 0.47 | 0.37 | 0.77 | 0.07 |
| **Train:2013-2018**<br>**Test:2018-2023**<br>**ALT** | 0.20 | 0.15 | 0.86 | -0.008 |
| **Train: 2018-2023**<br>**Test: 2013-2018**<br>**ALT** | 0.19 | 0.15 | 0.88 | 0.005 |

Environmental blocks were defined by clustering samples in covariate space using K-means (K=79). Model transferability was evaluated by holding out entire clusters during cross-validation. Domain of applicability was assessed using covariate-range coverage and nearest-neighbor distance–based familiarity metrics.

For MAGT in environmental-block validation and domain of applicability, the model achieved an average $R^2 = 0.40$ and RMSE = 0.63 °C, with negligible bias (–0.01 °C). Model performance across environmental clusters is reported in terms of $R^2$ and RMSE. For ALT, performance was comparable, with $R^2 = 0.41$ and RMSE = 0.35 m, also showing minimal bias. Some environmental blocks showed slightly lower accuracy due to greater climatic and soil differences, but overall transferability remained strong.

### 4.2 Spatial distribution of ALT

Vegetation and proximity to water bodies modulate thermal conditions: dense boreal vegetation provides insulation, while lakes and lowland terrain contribute to localized warming. ALT distributions mirror MAGT patterns (Fig. 4 in the Year-2 report), with shallower thaw depths (<1 m) in colder, sparsely vegetated areas and deeper seasonal thaw (>2 m) in warmer, lowland, or forested zones (Fig. 2). Permafrost in upland and interior tundra shows greater stability, whereas ALT thickens markedly along southern and southeastern edges of the region, areas prone to degradation. These maps highlight areas of high environmental variability, where local drivers such as vegetation type and ground ice content influence permafrost thermal regimes.

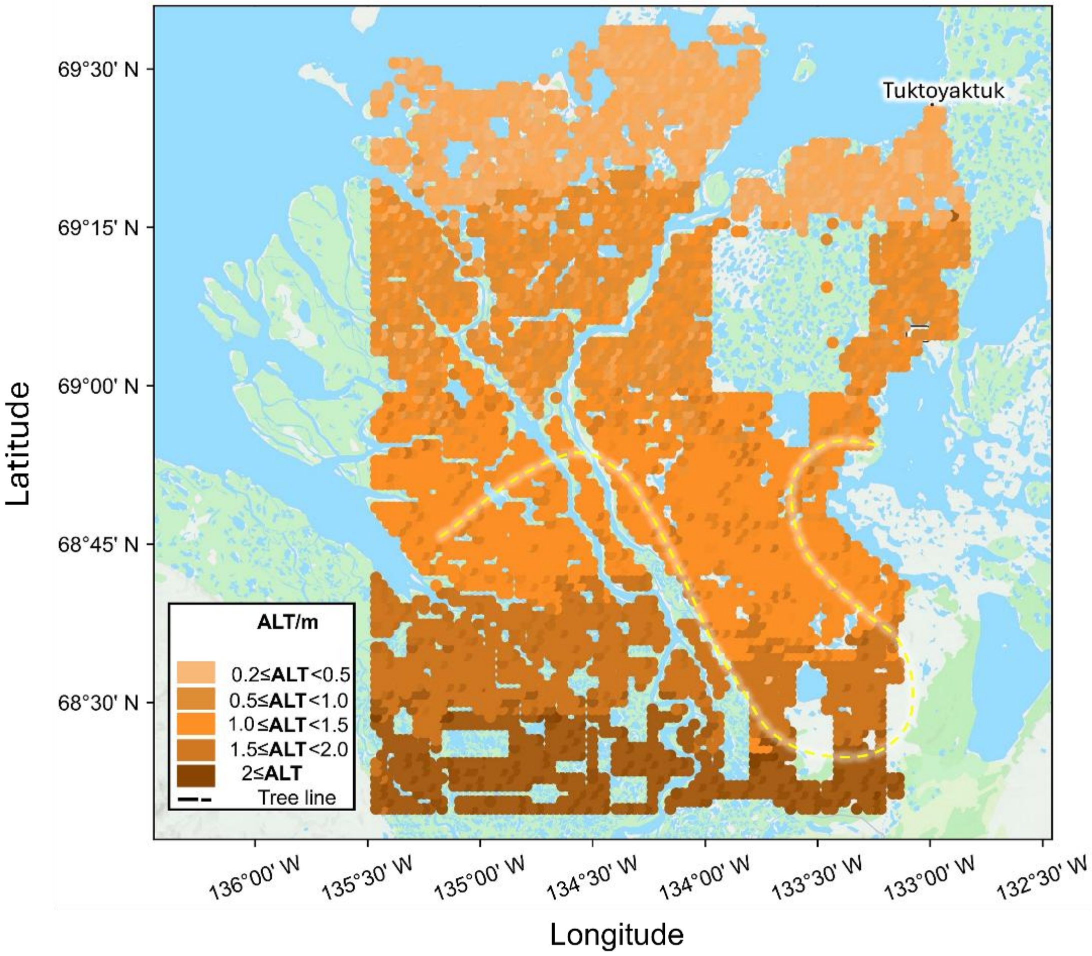

**Fig. 2**. ALT distribution, showing permafrost stability influenced by vegetation, water bodies, and climate. The yellow dashed line indicates the tree line limit.

To quantify spatial prediction uncertainty, we generated maps of the standard deviation (SD) for ALT using a k-nearest neighbours (kNN) approach. The SD reflects the variability among neighbouring samples in feature space and therefore serves as a neighborhood-based uncertainty proxy. Areas of higher uncertainty (SD>0.8 m) are concentrated near the tree line and in heterogeneous terrain, where snow cover, vegetation, and soil moisture vary rapidly over short distances (Fig 3). In contrast, SD is low (<0.3 m) across more homogeneous tundra and coastal zones, reflecting greater model confidence. ALT averaged 1.12 ± 0.56 m, with deeper seasonal thaws occurring in forested southern zones.

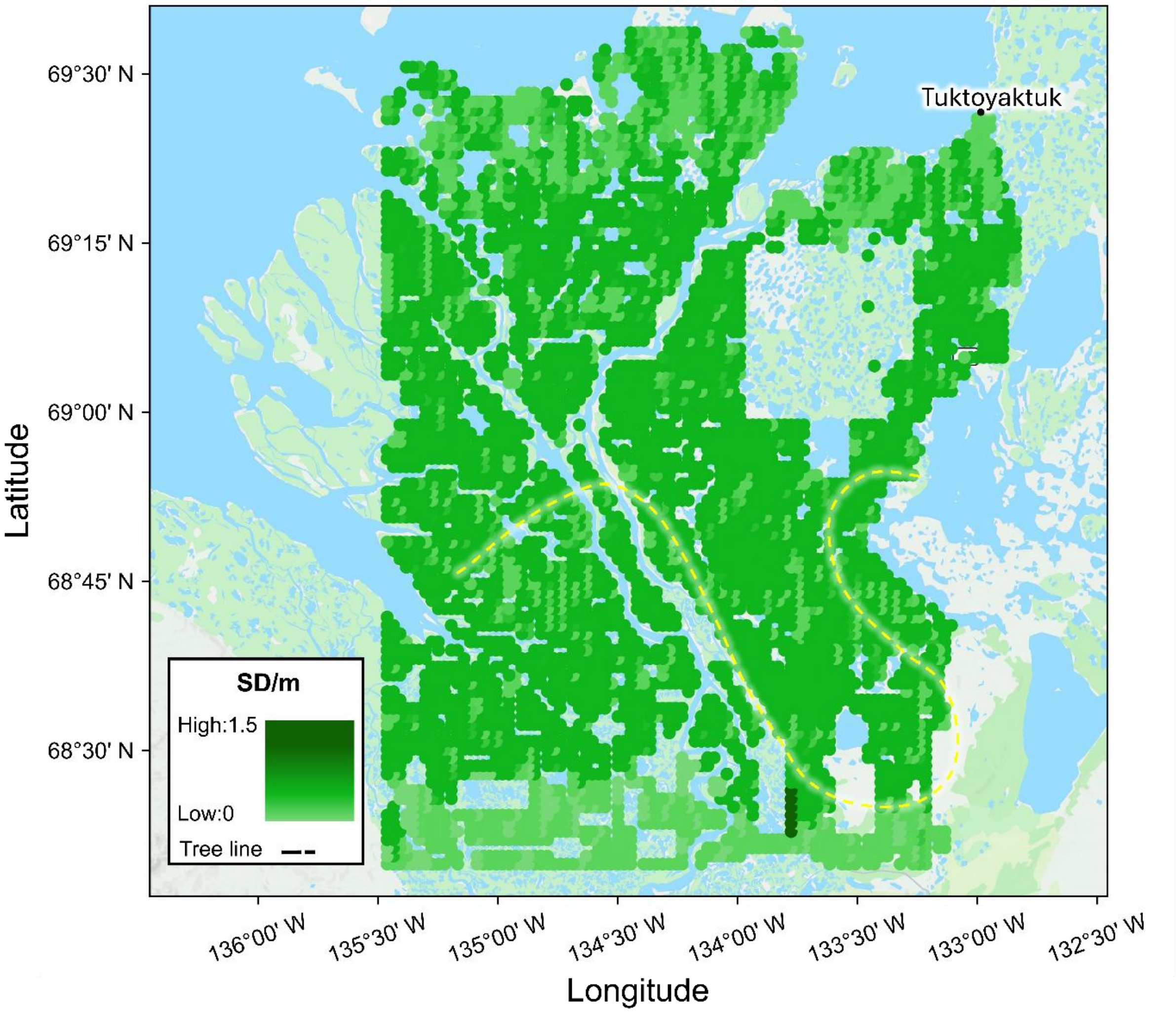

**Fig. 3.** SD of ALT from kNN. The SD map reflects a robust estimate of variability, ensuring that the final values are statistically reliable and capture the true range of temperature fluctuations across the study area.

### 4.3 Change between two five-year periods (2013–2018 vs 2018–2023)

We analyze two partially overlapping five-year windows (2013–2018 and 2018–2023) to maintain continuity and maximize coverage. The overlap (ending in 2018 and beginning at 2018) prevents an abrupt break in the record, and comparison across the two intervals shows a measurable regional shift toward warmer ground and deeper seasonal thaw. On average, MAGT increased by 0.28 °C (–3.11 °C to –2.83 °C) and ALT thickened by 0.22 m (1.22 m to 1.44 m). Annual rates were estimated by dividing the difference between the two five-year periods by the corresponding time interval, yielding rates of 0.056 °C $yr^{-1}$ and 0.044 m $yr^{-1}$, respectively. These changes mark a progressive decline in permafrost stability.

The strongest shifts cluster in the southern Mackenzie Delta and along the ITH corridor, where warm, ice-rich and water-influenced terrains exhibit transitions from colder MAGT classes (−5 to −4 °C) to warmer categories (>–3 °C) and from shallow to >2.0 m active layers. Landscape-specific patterns are also evident. In southern lowlands, MAGT rose from –2.2 °C to –1.6 °C and ALT deepened by ~0.4 m, especially near transportation corridors. In deltaic basins and floodplains, active layers increased from 1.5 m to more than 2.0 m, with concentrations around Trail Valley. Colder northern tundra plateaus (MAGT ~ –5.1 °C) remain largely stable but show localized warming up to +0.6 °C, indicating emerging change in otherwise resilient landscapes.

### 4.4 Permafrost hotspots and rate-based early warning indicators of thawing

Difference maps of MAGT and ALT between 2013–2018 and 2018–2023 (Fig. 4) reveal spatially explicit zones of rapid change. Areas where MAGT warmed beyond –2.5 °C or ALT exceeded 2.0 m cluster along the ITH and in the southern Mackenzie Delta, marking regions of heightened vulnerability for infrastructure and carbon flux. Importantly, hotspots were not limited to already warm permafrost; sites with initially low MAGT or shallow ALT also experienced accelerated change, indicating that rates of warming are as critical as thresholds for early detection of instability, a novel perspective that frames rate-based indicators as early warning tools for permafrost degradation.

This distinction is emphasized in rate-based heatmaps (Fig. 5) and bar plots (Fig. 6), which show that even areas still below freezing can be thermally unstable if warming trends are strong. Such regions are poised to cross degradation thresholds in the near future, amplifying risks of thermokarst, ecological transformation, and greenhouse gas release. Heatmaps act as rate-based early warning indicators and highlight spatial intensity, with shifts such as –5 to –4 °C or 0.5 to 1.0 m in ALT, underscoring emerging thaw hotspots. Averaged across the study area, MAGT increased from –3.11 °C to –2.83 °C and ALT from 1.22 m to 1.44 m (Fig. 6), confirming measurable rates of degradation over the past decade. Together, these analyses reveal that permafrost vulnerability is governed by both absolute thresholds and the pace of change, providing essential early warning indicators for risk monitoring in rapidly warming Arctic landscapes.

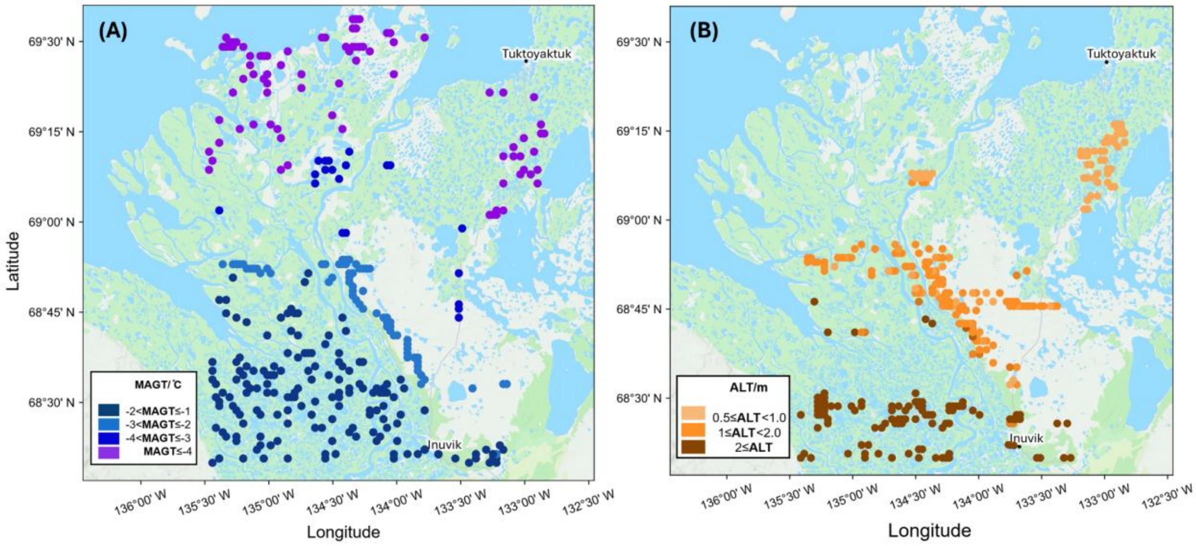

**Fig. 4**. **Spatial changes in MAGT (A) and ALT (B) between the 2013–2018 and 2018–2023 periods.** Maps display only locations exhibiting notable changes between the two intervals, illustrating spatial patterns of change across the MRD and the ITH corridor (Threshold: |ΔMAGT| > 0.28 °C; |ΔALT| > 0.22m).

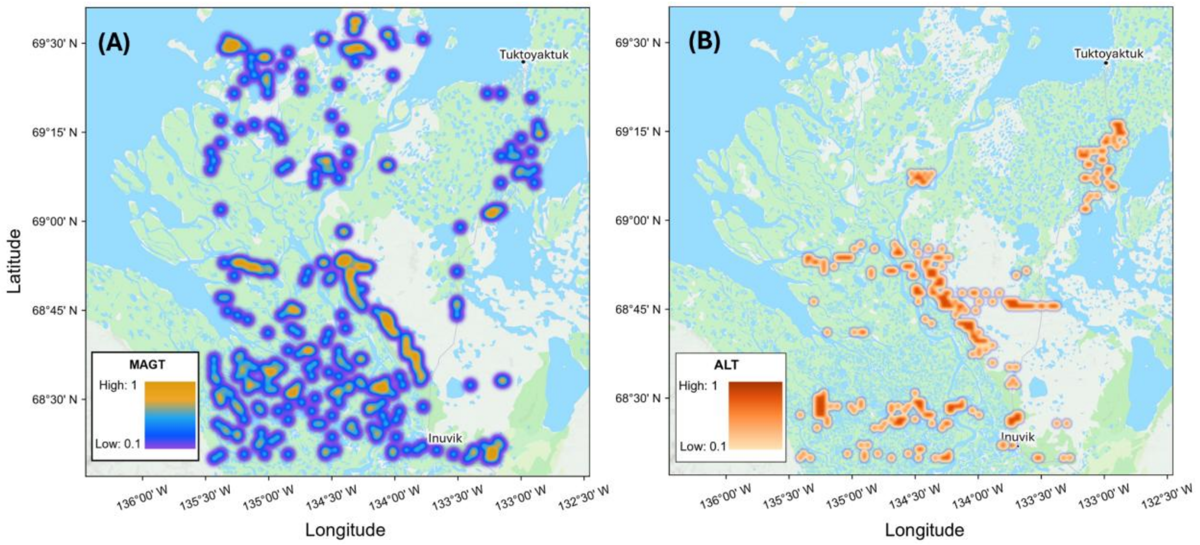

**Fig. 5. Heatmaps of change in MAGT (A) and ALT (B) between the 2013–2018 and 2018–2023 periods.** Differences (ΔMAGT and ΔALT) represent changes between the two intervals, emphasizing spatial patterns of magnitude rather than absolute values.

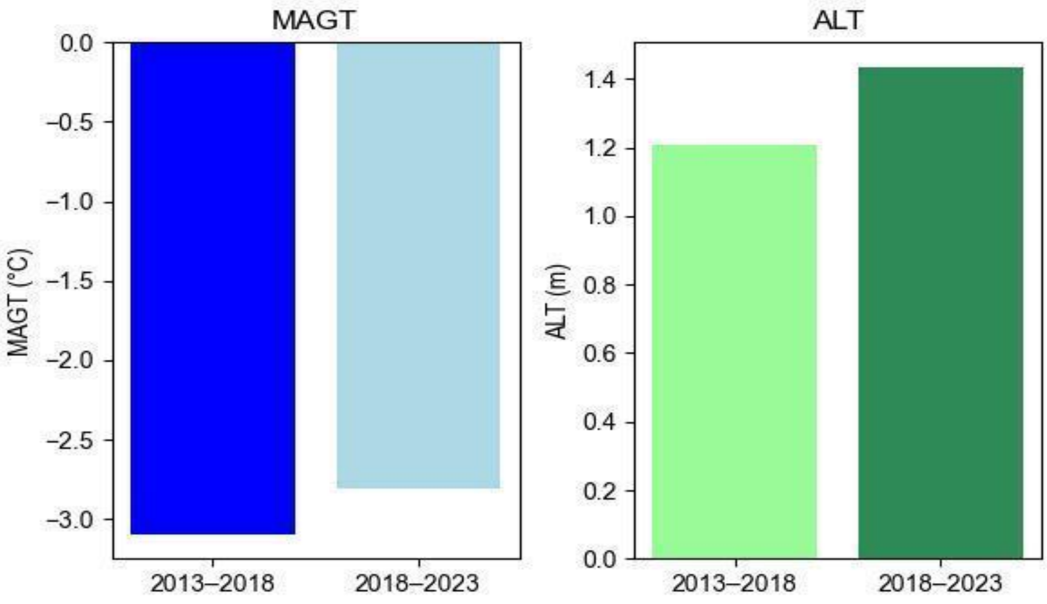

**Fig. 6. Region-mean changes in MAGT (A) and ALT(B) between the 2013–2018 and 2018–2023 periods.** Decadal differences and implied annual rates (~0.056 °C $yr^{-1}$ for MAGT; ~0.044 m $yr^{-1}$ for ALT) serve as rate-based indicators of warming and thaw progression, supporting baseline assessment of permafrost.

Thaw hotspots identified along the ITH corridor and southern Mackenzie Delta may indicate increased risk to drilling mud sumps that rely on frozen ground for containment. Deepening ALT and warming MAGT reduce the thickness and strength of the frozen barrier surrounding sump materials, potentially increasing permeability, ground subsidence, and contaminant mobility. Areas showing rapid warming rates represent emerging risk zones, even where permafrost remains below 0 °C. The ML-based hotspot maps, therefore, provide a practical tool for identifying sump locations that may require enhanced monitoring or mitigation under continued climate warming.

### 4.5 Model assumptions and predictive scope

Both RF and NNs models assume that the relationships between predictors and thermal state remain stationary across the mapping domain. This assumption may not hold in regions experiencing nonlinear or threshold behavior, such as rapid thermokarst development, vegetation shifts, or infrastructure-induced microclimatic effects. Additionally, the models rely on static environmental predictors and do not explicitly predict subsurface physical processes such as phase changes, latent heat effects, or lateral water flow. Consequently, while ML captures spatial variability and near-surface responses effectively, it does not reproduce subsurface thermodynamics or transient feedbacks that control long-term stability (29, 33, 75).

### 4.6 Sources and representation of uncertainty

Prediction uncertainty arises from three main components:
(1) Data uncertainty, due to measurement errors, limited sampling density, and interpolation of missing inputs (21, 24, 34, 35).
(2) Model uncertainty, linked to algorithm selection, feature interactions, and limited training diversity.
(3) Environmental uncertainty, reflecting natural heterogeneity of terrain, vegetation, and snow cover.

Our kNN based uncertainty map partially quantify these effects, showing elevated standard deviation (>0.8 m) near the tree line and transition zones where snow and vegetation variability are high. In contrast, homogeneous tundra and coastal regions exhibit lower uncertainty (<0.3 m), reflecting higher predictive confidence. These spatial uncertainty patterns provide a probabilistic context for interpreting the maps, highlighting regions where results represent robust patterns versus those that require targeted field validation (58).

### 4.7 Bounding claims and interpretive caution

Given the data and model constraints, our results should be viewed as regionally representative but not absolute depictions of the ground thermal state. The derived warming rates (0.056 °C $yr^{-1}$ for MAGT; 0.044 °C $yr^{-1}$ for ALT) describe average trends within the monitoring footprint and may differ locally due to unobserved microclimates or disturbances. Extrapolation beyond the trained domain, especially into unmonitored portions of the delta or adjacent physiographic regions, should be done cautiously (10, 21, 29, 47, 52).

## 5. Future work

The objectives of this study have been substantially completed. The next phase will focus on quantifying permafrost thaw under different climate change scenarios.

Future work will expand the modelling framework through integration of additional datasets, including new in situ ground measurements, advanced remote sensing products, and updated climate reanalysis data. Incorporating these complementary data sources will enhance prediction accuracy, improve spatial generalizability, and enable cross-validation beyond the original training corridor. Uncertainty quantification will be systematically strengthened through ensemble modelling strategies and probabilistic outputs derived from Neural Networks, allowing explicit estimation of confidence intervals and improving the reliability of predictions for decision-making applications.

To address long-term climate impacts, future projections will incorporate Representative Concentration Pathway (RCP) scenarios, including RCP2.6, RCP4.5, RCP6.0, and RCP8.5. These scenarios represent alternative greenhouse gas emission trajectories and associated climate responses. Downscaled climate projections extending from historical baselines to 2100 (and where available, to 2300) have already been compiled for key variables, including mean air temperature, maximum and minimum near-surface air temperature, precipitation, and snow depth. These datasets provide the necessary inputs to drive scenario-based predictions of future MAGT and ALT.

Using these projections, the ML framework will be applied to estimate long-term changes in permafrost thermal state and active layer dynamics under different emission pathways. This will enable scenario-based risk assessments of permafrost degradation, including evaluation of hazards such as ground subsidence, infrastructure vulnerability, carbon release, and impacts on drilling mud sumps. Furthermore, spatial and temporal variability in permafrost response across scenarios will be analyzed to examine how thaw trajectories evolve over decadal to centennial timescales.

Overall, integrating data-driven modelling, environmental sensitivity analysis, and climate scenario projections will significantly enhance our capacity to anticipate, quantify, and manage the multifaceted impacts of permafrost thaw across northern landscapes.

## References

1. W. Dobinski, Permafrost. *Earth-Sci. Rev.* **108**, 158–169 (2011).
2. S. V. Kokelj, T. Gingras-Hill, S. V. Daly, P. D. Morse, S. A. Wolfe, A. C. Rudy, et al., The Northwest Territories Thermokarst Mapping Collective: A northern-driven mapping collaborative toward understanding the effects of permafrost thaw. *Arctic Sci.* **9**, 886–918 (2023).
3. M. C. Jones, G. Grosse, C. Treat, M. Turetsky, K. W. Anthony, L. Brosius, Past permafrost dynamics can inform future permafrost carbon–climate feedbacks. *Commun. Earth Environ.* **4**, 272 (2023).
4. T. J. Bouffard, E. Uryupova, K. Dodds, V. E. Romanovsky, A. P. Bennett, D. Streletskiy, Scientific cooperation: Supporting circumpolar permafrost monitoring and data sharing. *Land* **10**, 590 (2021).
5. T. Schneider von Deimling, H. Lee, T. Ingeman-Nielsen, S. Westermann, V. Romanovsky, S. Lamoureux, et al., Consequences of permafrost degradation for Arctic infrastructure—bridging the model gap between regional and engineering scales. *The Cryosphere* **15**, 2451–2471 (2021).
6. S. L. Smith, H. B. O'Neill, K. Isaksen, J. Noetzli, V. E. Romanovsky, The changing thermal state of permafrost. *Nat. Rev. Earth Environ.* **3**, 10–23 (2022).
7. K. Schaefer, H. Lantuit, V. E. Romanovsky, E. A. Schuur, R. Witt, The impact of the permafrost carbon feedback on global climate. *Environ. Res. Lett.* **9**, 085003 (2014).
8. E. A. Schuur, A. D. McGuire, C. Schädel, G. Grosse, J. W. Harden, D. J. Hayes, et al., Climate change and the permafrost carbon feedback. *Nature* **520**, 171–179 (2015).
9. S. E. Chadburn, E. J. Burke, P. M. Cox, P. Friedlingstein, G. Hugelius, S. Westermann, An observation-based constraint on permafrost loss as a function of global warming. *Nat. Clim. Change* **7**, 340–344 (2017).
10. B. K. Biskaborn, S. L. Smith, J. Noetzli, et al., Permafrost is warming at a global scale. *Nat. Commun.* **10**, 264 (2019).
11. D. Luo, Q. Wu, H. Jin, S. S. Marchenko, L. Lü, S. Gao, Recent changes in the active layer thickness across the Northern Hemisphere. *Environ. Earth Sci.* **75**, 1–15 (2016).
12. X. Y. Jin, H. J. Jin, G. Iwahana, S. S. Marchenko, D. L. Luo, X. Y. Li, S. H. Liang, Impacts of climate-induced permafrost degradation on vegetation: A review. *Adv. Clim. Change Res.* **12**, 29–47 (2021).
13. C. C. Treat, M. C. Jones, J. Alder, A. B. K. Sannel, P. Camill, S. Frolking, Predicted vulnerability of carbon in permafrost peatlands with future climate change and permafrost thaw in western Canada. *J. Geophys. Res. Biogeosci.* **126**, e2020JG005872 (2021).
14. S. V. Daly, P. P. Bonnaventure, W. Kochtitzky, Influence of ecosystem and disturbance on near-surface permafrost distribution, Whatì, Northwest Territories, Canada. *Permafr. Periglac. Process.* **33**, 339–352 (2022).

15. C. M. Dieleman, N. J. Day, J. E. Holloway, J. Baltzer, T. A. Douglas, M. R. Turetsky, Carbon and nitrogen cycling dynamics following permafrost thaw in the Northwest Territories, Canada. *Sci. Total Environ.* **845**, 157288 (2022).
16. D. K. Swanson, P. J. Sousanes, K. Hill, Increased mean annual temperatures in 2014–2019 indicate permafrost thaw in Alaskan national parks. *Arct. Antarct. Alp. Res.* **53**, 1–19 (2021).
17. J. He, K. Yang, W. Tang, H. Lu, J. Qin, Y. Chen, X. Li, The first high-resolution meteorological forcing dataset for land process studies over China. *Sci. Data* **7**, 25 (2020).
18. M. C. Garibaldi, P. P. Bonnaventure, S. L. Smith, C. Duchesne, Active layer variability and change in the Mackenzie Valley, Northwest Territories between 1991–2014: An ecoregional assessment. *Arct. Antarct. Alp. Res.* **54**, 274–293 (2022).
19. E. L. Ogden, S. G. Cumming, S. L. Smith, M. R. Turetsky, J. L. Baltzer, Permafrost thaw induces short-term increase in vegetation productivity in northwestern Canada. *Glob. Change Biol.* **29**, 5352–5366 (2023).
20. L. Zhao, C. Xie, D. Yang, T. Zhang, Ground temperature and active layer regimes and changes. In *Arctic Hydrology, Permafrost and Ecosystems* (Springer, 2021), pp. 441–470.
21. H. B. O'Neill, S. L. Smith, C. R. Burn, C. Duchesne, Y. Zhang, Widespread permafrost degradation and thaw subsidence in Northwest Canada. *J. Geophys. Res. Earth Surf.* **128**, e2023JF007262 (2023).
22. M. T. Jorgenson, V. Romanovsky, J. Harden, Y. Shur, J. O'Donnell, E. A. Schuur, et al., Resilience and vulnerability of permafrost to climate change. *Can. J. For. Res.* **40**, 1219–1236 (2010).
23. L. Orgogozo, A. S. Prokushkin, O. S. Pokrovsky, C. Grenier, M. Quintard, J. Viers, S. Audry, Water and energy transfer modeling in a permafrost-dominated, forested catchment of Central Siberia: The key role of rooting depth. *Permafr. Periglac. Process.* **30**, 75–89 (2019).
24. J. Nitzbon, S. Westermann, M. Langer, L. C. P. Martin, J. Strauss, S. Laboor, J. Boike, Fast response of cold ice-rich permafrost in northeast Siberia to a warming climate. *Nat. Commun.* **11**, 2201 (2020).
25. I. Nadeem, N. Nakicenovic, A. Yaqub, B. Sakschewski, S. Loriani, G. Bala, et al., Permafrost thawing and estimates of vulnerable carbon in the northern high latitudes. Earth Syst. Environ. (2024).
26. B. R. Bonsal, B. Kochtubajda, An assessment of present and future climate in the Mackenzie Delta and the near-shore Beaufort Sea region of Canada. *Int. J. Climatol.* **29**, 1780–1795 (2009).
27. K. Kohnert, A. Serafimovich, S. Metzger, J. Hartmann, T. Sachs, Strong geologic methane emissions from discontinuous terrestrial permafrost in the Mackenzie Delta, Canada. *Sci. Rep.* **7**, 5828 (2017).
28. J. Hjort, O. Karjalainen, J. Aalto, S. Westermann, V. E. Romanovsky, F. E. Nelson, et al., Degrading permafrost puts Arctic infrastructure at risk by mid-century. *Nat. Commun.* **9**, 5147 (2018).
29. Y. Qin, T. Wu, L. Zhao, X. Wu, R. Li, C. Xie, et al., Numerical modeling of the active layer thickness and permafrost thermal state across the Qinghai–Tibetan Plateau. *J. Geophys. Res. Atmos.* **122**, 11,604–11,620 (2017).
30. J. Perreault, R. Fortier, J. W. Molson, Numerical modelling of permafrost dynamics under climate change and evolving ground surface conditions: Application to an instrumented permafrost mound at Umiujaq, Nunavik (Québec), Canada. *Écoscience* **28**, 377–397 (2021).

31. S. Westermann, T. Ingeman-Nielsen, J. Scheer, K. Aalstad, J. Aga, N. Chaudhary, et al., The CryoGrid community model (version 1.0)—a multi-physics toolbox for climate-driven simulations in the terrestrial cryosphere. *Geosci. Model Dev.* **16**, 2607–2647 (2023).
32. S. L. Painter, E. T. Coon, A. L. Atchley, M. Berndt, R. Garimella, J. D. Moulton, et al., Integrated surface/subsurface permafrost thermal hydrology: Model formulation and proof-of-concept simulations. *Water Resour. Res.* **52**, 6062–6077 (2016).
33. S. Karra, S. L. Painter, P. C. Lichtner, Three-phase numerical model for subsurface hydrology in permafrost-affected regions (PFLOTRAN-ICE v1.0). *The Cryosphere* **8**, 1935–1950 (2014).
34. R. Chance, A. Ahajjam, J. Putkonen, T. Pasch, Artificial intelligence for predicting Arctic permafrost and active layer temperatures along the Alaskan North Slope. *Earth Sci. Inform.* (2024).
35. R. Li, M. Zhang, W. Pei, A. Melnikov, Z. Zhang, G. Li, Risk evaluation of thaw settlement using machine learning models for the Wudaoliang–Tuotuohe region, Qinghai–Tibet Plateau. *Catena* **220**, 106700 (2023).
36. G. Yin, J. Luo, F. Niu, Z. Lin, M. Liu, Machine learning-based thermokarst landslide susceptibility modeling across the permafrost region on the Qinghai–Tibet Plateau. *Landslides* **18**, 2639–2649 (2021).
37. D. Wheeler, G. Shaw, S. Barr, *Statistical Techniques in Geographical Analysis*, Chap. 9 (Routledge, 2013).
38. D. Rolnick, P. L. Donti, L. H. Kaack, K. Kochanski, A. Lacoste, K. Sankaran, et al., Tackling climate change with machine learning. *ACM Comput. Surv.* **55**, 1–96 (2022).
39. S. V. Kokelj, M. J. Palmer, T. C. Lantz, C. R. Burn, Ground temperatures and permafrost warming from forest to tundra, Tuktoyaktuk Coastlands and Anderson Plain, NWT, Canada. *Permafr. Periglac. Process.* **28**, 543–551 (2017).
40. C. A. Rudy, S. V. Kokelj, P. D. Morse, T. Ensom, Permafrost ground temperature report: Inuvik to Tuktoyaktuk Highway sentinel sites, Northwest Territories. Northwest Territories Geological Survey, Open Rep. 2019-017 (2019).
41. Meteorological Service of Canada, Government of Canada, https://weather.gc.ca.
42. Environment and Climate Change Canada, Canadian climate normals 1981–2010. Government of Canada, https://climate.weather.gc.ca/climate_normals/ (accessed 22 July 2025).
43. T. Ensom, P. D. Morse, S. V. Kokelj, E. MacDonald, J. Young, S. Tank, R. Subedi, E. Grozic, A. Castagner, Permafrost geotechnical borehole data synthesis: Inuvik–Tuktoyaktuk region, Northwest Territories. *Geol. Surv. Can.*, Open File 8652 (2019), doi:10.4095/321869.
44. J. R. Mackay, Permafrost depths, lower Mackenzie Valley, Northwest Territories. *Arctic* **20**, 21–26 (1967).
45. S. Judge, A. E. Taylor, M. Burgess, Canadian geothermal data collection—Northern wells 1977–1978. Geothermal Series No. 11, Earth Physics Branch, Energy, Mines and Resources (1979).
46. H. MacDougall, Estimated effect of the permafrost carbon feedback on the zero emissions commitment to climate change. *Biogeosciences* **18**, 4937–4952 (2021).
47. T. Ensom, S. V. Kokelj, P. D. Morse, K. Kamo McHugh, Permafrost ground temperature data synthesis: 2013–2019 Inuvik–Tuktoyaktuk Highway region, Northwest Territories. Geol. Surv. Can., Open File 8656 (2020), doi:10.4095/321870.
48. Geological Survey of the Northwest Territories, NWT geoscience data hub. Government of the Northwest Territories, https://app.nwtgeoscience.ca/ (accessed 22 July 2025).
49. ISRIC – World Soil Information, SoilGrids—global gridded soil information, https://soilgrids.org (accessed 22 July 2025).

50. Fatolahzadeh Gheysari, P. Maghoul, A framework to assess permafrost thaw threat for land transportation infrastructure in northern Canada. Commun. Earth Environ. 5, 167 (2024).
51. H. Sarker, Machine learning: Algorithms, real-world applications, and research directions. SN Comput. Sci. 2, 160 (2021).
52. J. Boike, S. Chadburn, J. Martin, S. Zwieback, I. H. Althuizen, N. Anselm, et al., Standardized monitoring of permafrost thaw: A user-friendly, multiparameter protocol. Arctic Sci. 8, 153–182 (2021).
53. M. A. Merchant, L. McBlane, Machine learning-based active layer thickness estimation over permafrost landscapes by upscaling airborne remote sensing measurements with cloud-computing geotechnologies. In *Machine Learning Applications in Earth Observation* (IntechOpen, 2024).
54. Karpatne, I. Ebert-Uphoff, S. Ravela, H. A. Babaie, V. Kumar, Machine learning for geosciences: Challenges and opportunities. IEEE Trans. Knowl. Data Eng. 31, 1544–1554 (2018).
55. H. Park, K. Kim, D. K. Lee, Prediction of severe drought areas based on random forest using satellite imagery and topographic data. Water 11, 705 (2019).
56. J. Ni, T. Wu, X. Zhu, G. Hu, D. Zou, X. Wu, et al., Simulation of the present and future projection of permafrost on the Qinghai–Tibet Plateau with statistical and machine learning models. *J. Geophys. Res. Atmos.* **126**, e2020JD033402 (2021).
57. L. Breiman, Random forests. Mach. Learn. 45, 5–32 (2001).
58. V. Y. Kulkarni, P. K. Sinha, Pruning of random forest classifiers: A survey and future directions. In Proc. Int. Conf. Data Science & Engineering (ICDSE) (IEEE, 2012), pp. 64–68, doi:10.1109/ICDSE.2012.6282329.
59. Y. Wang, X. Chen, M. Gao, J. Dong, Use of random forest to identify climate and human interference on vegetation coverage changes in southwest China. Ecol. Indic. 144, 109463 (2022).
60. Q. Liu, J. Niu, P. Lu, F. Dong, F. Zhou, X. Meng, et al., Interannual and seasonal variations of permafrost thaw depth on the Qinghai–Tibet Plateau: A comparative study using long short-term memory, convolutional neural networks, and random forest. Sci. Total Environ. 838, 155886 (2022).
61. Z. Ma, Z. Liu, J. Pu, L. Xu, K. Li, L. Wangqu, et al., Deep convolutional neural network with random field model for lake ice mapping from Sentinel-1 imagery. Int. J. Remote Sens. 42, 9351–9375 (2021).
62. P. Baral, M. A. Haq, Spatial prediction of permafrost occurrence in the Sikkim Himalayas using logistic regression, random forests, support vector machines, and neural networks. Geomorphology 371, 107331 (2020).
63. H. Cai, C. Wang, Z. Ma, F. Meng, Z. Lin, J. Ren, S. Li, Predicting frost heave in soil–water systems using a generalized regression neural network optimized with particle swarm optimization. Cold Reg. Sci. Technol. 226, 104291 (2024).
64. C. Zhang, T. A. Douglas, J. E. Anderson, Modeling and mapping permafrost active layer thickness using field measurements and remote sensing techniques. Int. J. Appl. Earth Obs. Geoinf. 102, 102455 (2021).
65. V. Glinskikh, O. Nechaev, I. Mikhaylov, M. Nikitenko, K. Danilovskiy, Transient electromagnetic monitoring of permafrost: Mathematical modeling based on Sumudu integral transform and artificial neural networks. Mathematics 12, 585 (2024).
66. T. Chang, Y. Yi, H. Jiang, R. Li, P. Lu, L. Liu, et al., Unraveling the nonlinear relationship between seasonal deformation and permafrost active layer thickness. npj Clim. Atmos. Sci. 7, 308 (2024).